









## Effect of the shot-to-shot variation on charge migration induced by sub-fs x-ray free-electron laser pulses

Gilbert Grell <sup>1,2,\*</sup> Zhaoheng Guo <sup>3,4</sup> Taran Driver <sup>4,5</sup> Piero Decleva <sup>6,7</sup> Etienne Plésiat,<sup>1,2</sup> Antonio Picón <sup>2</sup>  
 Jesús González-Vázquez <sup>2,8</sup> Peter Walter,<sup>4</sup> Jonathan P. Marangos <sup>9</sup> James P. Cryan,<sup>4,5</sup> Agostino Marinelli,<sup>3,4</sup>  
 Alicia Palacios <sup>2,8</sup> and Fernando Martín<sup>1,2,10,†</sup>

<sup>1</sup>*Instituto Madrileño de Estudios Avanzados en Nanociencia (IMDEA-Nanociencia), Madrid 28049, Spain*

<sup>2</sup>*Departamento de Química, Universidad Autónoma de Madrid, Madrid 28049, Spain*

<sup>3</sup>*Stanford University, Stanford, California 94305, USA*

<sup>4</sup>*SLAC National Accelerator Laboratory, Menlo Park, California 94025, USA*

<sup>5</sup>*Stanford PULSE Institute, SLAC National Accelerator Laboratory, Menlo Park, California 94025, USA*

<sup>6</sup>*Istituto Officina dei Materiali (CNR-IOM), 34149 Basovizza - Trieste, Italy*

<sup>7</sup>*Dipartimento di Scienze Chimiche e Farmaceutiche, Università di Trieste, 34127 Trieste, Italy*

<sup>8</sup>*Institute for Advanced Research in Chemistry (IAdChem), Universidad Autónoma de Madrid, Madrid 28049, Spain*

<sup>9</sup>*The Blackett Laboratory Extreme Light Consortium, Imperial College London, London SW7 2AZ, United Kingdom*

<sup>10</sup>*Condensed Matter Physics Center (IFIMAC), Universidad Autónoma de Madrid, Madrid 28049, Spain*



(Received 20 December 2021; accepted 28 March 2023; published 11 May 2023)

X-ray free-electron lasers (XFELs) are now able to provide tunable pairs of intense sub-fs pulses in the soft x-ray regime, paving the way for time-resolved investigations of attosecond charge migration in molecules. However, the stochastic shot-to-shot variation of the XFEL pulses may degrade and eventually hide the observable features. We show by means of state-of-the-art calculations that the damping of the charge migration induced by 260 eV pulses in p-aminophenol due to the shot-to-shot variation of pulses generated at the Linac Coherent Light Source is negligible in comparison to the natural damping due to the intrinsic fluctuation of the initial molecular geometry. This result gives us confidence in the utility of XFEL sub-fs pulses for the measurement of charge migration and other ultrafast charge dynamics.

DOI: [10.1103/PhysRevResearch.5.023092](https://doi.org/10.1103/PhysRevResearch.5.023092)

### I. INTRODUCTION

Investigation of the early stages of intramolecular charge transfer induced by light is the first step towards understanding photochemical reactions [1–4], such as those occurring, e.g., in photosynthesis [5], photovoltaic [6], and molecular electronic devices [7], or biological radiation damage [8,9]. These early stages occur in the sub-fs to the few-fs time scale, access to which has provided a major boost to attosecond sciences [10–13] and given birth to “attochemistry” [14–19].

Since the synthesis of the first extreme ultraviolet (XUV) attosecond laser pulses through high harmonic generation (HHG) in noble gases [20,21], the progress in attosecond science has been closely connected to the advance in the construction of ever better HHG sources [10,11,13,17,22,23]. This allowed for the first attosecond-resolved observations of proton rearrangements [24] and sub-fs charge migration

dynamics in molecules [14,25–29], the reconstruction of the electronic wave packets in real time [30,31], and the attosecond control of simple fragmentation reactions [32–36]. Most of these works employ either (i) a pump-probe scheme consisting of an isolated or a train of attosecond XUV pulses in combination with the few-fs near infrared (NIR) driving field [14,26,28,32,33], (ii) NIR pulses with a tunable carrier envelope phase [25,34,36], or (iii) intense NIR pulses enabling attosecond probing via spectroscopy of the generated harmonics [24,27,29,30]. Therein, the NIR pulses can, depending on their intensity, drive multiphoton transitions and nonperturbative strong field dynamics that complicate the experimental analysis as well as theoretical modeling and may eventually hide the original dynamics induced by the gentle pump pulse.

This issue can be circumvented by changing to XUV-only attosecond pump-probe schemes [12,15,18,19]. Unfortunately, due to the intensity drop in the generation of higher harmonics [37], this route still remains a formidable challenge and only a few experimental sub-fs XUV pump-probe setups and applications have been reported so far [31,38–40]. Since the decrease in the harmonics’ intensities is even more dramatic at higher photon energies, realization of nonlinear attosecond soft x-ray (SXR) spectroscopic methods [41,42], which have been identified as versatile probes of transient effects in molecules [43–50], is still awaiting its advent, though

\*gilbert.grell@imdea.org

†fernando.martin@uam.es

modern HHG sources can already provide pulses shorter than 100 as above the oxygen K-edge [23,51–55].

X-ray free-electron lasers (XFELs), which are the brightest sources of coherent x-ray radiation available today [56–61], in turn deliver the intensities required for few-fs x-ray pump-probe measurements [62] and very recently have been demonstrated to reach sub-fs pulse durations in the SXR regime [63]. In the latter work, a split-undulator setup [64] was used to generate tunable pairs of isolated two-color sub-fs SXR pulses at controllable attosecond time delays with intensities exceeding those obtained from state of the art SXR HHG sources by many orders of magnitude. This breakthrough has paved the way to conduct attosecond-resolved SXR spectroscopies. However, in contrast to HHG sources, attosecond XFELs operating according to the self-amplified spontaneous emission (SASE) principle build up the pulses from noise, leading to a stochastic shot-to-shot variation of the pulse properties [65]. For example, the pulse energy, bandwidth, and duration of sub-fs SXR pulses have been measured to fluctuate by a significant fraction of their mean [63]. In two-color sub-fs pump/sub-fs probe schemes both pulses are seeded from noise and are therefore both subject to the shot-to-shot fluctuations of attosecond SASE XFELs. The intrinsic fluctuations of the probe pulse can be exploited in correlation-based methods to efficiently resolve spectral features in absorption [66] or photoemission spectroscopy measurements [50,67]. The effect of noise fluctuations in the pump pulse, however, is potentially more detrimental. Since the properties of the wavepacket launched by the pump pulse depend on the exact shape of its radiation field, averaging single-shot measurements for an ensemble of XFEL pulses can introduce a damping of the observable features. The impact of this problem, which is intrinsic to all currently available SASE XFELs, on charge migration studies is not yet known. This is particularly important, since sub-fs SXR pulses create coherent superpositions of large manifolds of electronic states [18] leading to delocalized charge fluctuations all over the molecule [13,14,19,68–72], in contrast with directional charge migration resulting from sudden ionization of single [4,73–75] or few [76–79] molecular orbitals. In principle, the impact of the x-ray pulse fluctuations can be circumvented by monitoring and binning data on the x-ray properties of each pump-pulse. Since such an approach is data intensive, we ask if physically incisive measurements of charge migration are viable without this.

In this paper, we investigate the effect of XFEL shot-to-shot variations on the charge migration induced by sub-fs SXR pulses in the para-aminophenol (p-aminophenol) molecule by performing theoretical calculations of the ionization amplitudes for an ensemble of realistic sub-fs 260 eV pulses that represent those produced at the Linac Coherent Light Source (LCLS) [63]. p-aminophenol is an ideal benchmark because it comprises an amino (NH<sub>2</sub>) and a hydroxy (OH) group at opposite ends of a stable C<sub>6</sub>H<sub>4</sub> aromatic ring (NH<sub>2</sub>-C<sub>6</sub>H<sub>4</sub>-OH), allowing for selective x-ray spectroscopic probing of the charge migration at the oxygen and nitrogen sites. We show that, for a given molecular geometry, the shot-to-shot variation affects the charge fluctuations induced in different molecular sites by no more than 35% during the first 10 fs after ionization by the pump pulses. To place this effect

in perspective, we compare it with the impact of the geometric variations due to the nonzero width of the ground-state nuclear wave function of p-aminophenol at 300 K. As predicted by earlier theoretical work [76,77], already the nuclear zero-point energy, which is common to any molecule and thus affects any experimental measurement, may eventually damp the generated coherent charge dynamics at sufficiently long times. We show that, in particular beyond 3 fs, this effect is far more pronounced than that due to the XFEL shot-to-shot variation.

## II. SIMULATION APPROACH

### A. Shot-to-shot variation

We represent the shot-to-shot variation by an ensemble of 100 sub-fs XFEL pulses with a carrier frequency of  $\omega_0 = 260$  eV,

$$E(t) = |G(t)| \cos(\omega_0 t + \arg[G(t)]). \quad (1)$$

Each pulse in this ensemble is defined by its envelope function  $G(t) = |G(t)| \exp\{i \arg[G(t)]\}$  obtained from start-to-end simulations of the x-ray laser-enhanced attosecond pulse generation (XLEAP) procedure implemented at the LCLS [63]. Therein we used ELEGANT [80] to track the electron bunch until the start of the undulator beamline. A photocathode modulation [81] was employed to produce the short current spike. For this beam, time-dependent simulations of the FEL were performed by using the fully 3D code GENESIS 1.3 [82], wherein the undulator taper was matched with the energy chirp of the short current spike to generate single-spike 260 eV pulses. The variations in the properties of the individual pulses are obtained by using the same electron distribution with a re-initiated numerical shot-noise generator for each of the 100 XLEAP simulations. In that way we account for the natural shot-noise-induced variations in the pulse properties [63,65] and disregard the jitter in the macroscopic electron beam properties, e.g., mean energy and peak current. However, these properties can easily be measured on a shot-to-shot basis, allowing to remove their fluctuation from an experimental measurement during the data analysis. Furthermore, this effect is expected to be negligible compared to the shot-noise fluctuations in state of the art normal conducting accelerators [61,83] and next-generation superconducting accelerators [84].

The so-obtained ensemble of pulses has an averaged pulse energy of  $\mathcal{E}_{\text{avg}}^{\text{pulse}} = 42.8 \pm 18$   $\mu\text{J}$  and a temporal full width at half maximum (FWHM) of the power envelope  $|G(t)|^2$  of  $646 \pm 311$  as. The variation within the ensemble is illustrated in Fig. 1(a) for the absolute values and phases of the envelope function, while the respective pulse energy histogram is depicted in Fig. 1(b). The overlay of all envelopes yields a broad three-peak structure. It deviates considerably from the envelope of a Gaussian transform-limited pulse that approximately fits to the dominant spike of the ensemble at 4.0 fs with a FWHM duration of 0.85 fs [0.60 fs of  $|G(t)|^2$ ]. Coupled with a sinusoidal carrier wave, i.e. constant phase  $-\frac{\pi}{2}$ , this pulse serves herein as reference for the shot-to-shot variation. The phases of the simulated XFEL pulses have an approximately parabolic time dependence, covering several full periods within the sample. We note here that the aligned

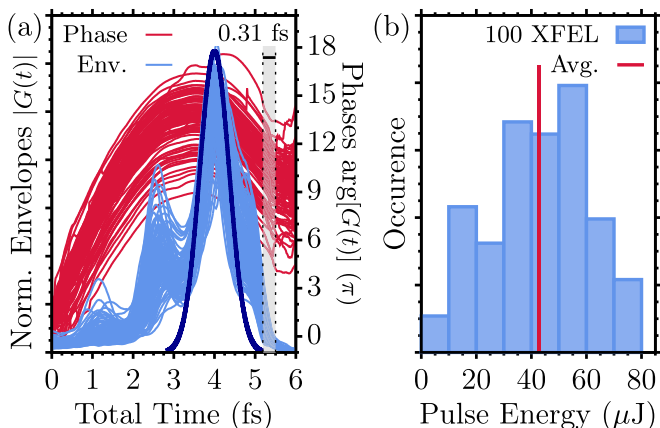


FIG. 1. (a) Normalized absolute values (blue) and phases (red) of the envelope functions  $G(t)$  of the 100 start-to-end simulated XFEL pulses. The thick blue line depicts the envelope of the 0.85 fs Gaussian transform-limited pulse, aligned with the main maximum of the XFEL pulse ensemble. The difference of 0.31 fs between the starting points of the free evolution at 5.19 fs (aligned Gaussian pulse) and 5.5 fs (XFEL pulses) is indicated with a transparent gray rectangle. (b) Pulse energy distribution of the 100 simulated XFEL pulses around the average of 42.8  $\mu\text{J}$  (red).

Gaussian pulse decays to zero at 5.19 fs, while the envelopes of the simulated pulses have considerable contributions until 5.5 fs and a tail until 6.0 fs. The latter part is neglected herein so that the free propagation obtained with the Gaussian pulse commences just 0.31 fs ahead of the ones obtained from the XFEL pulses.

### B. Ground-state nuclear effects

The effect of the ground-state nuclear wave function of *p*-aminophenol is herein represented by averaging the results over an ensemble of geometric configurations sampled from the harmonic ground-state Wigner distribution of the molecule, which has been found to be preferred over a purely thermal sampling [85]. By sampling 106 geometries directly from the finite temperature Wigner distribution comprising  $N_m = 39$  normal modes  $\xi$ , with dimensionless normal mode frequencies  $\omega_\xi$ , positions  $Q_\xi$  and momenta  $P_\xi$ ,

$$W(\mathbf{Q}, \mathbf{P}, T) = \prod_{\xi=1}^{N_m} \frac{\exp\left\{-\frac{(Q_\xi^2 + P_\xi^2)}{\coth\frac{\omega_\xi}{2k_B T}}\right\}}{\pi \coth\frac{\omega_\xi}{2k_B T}}, \quad (2)$$

we take into account its nuclear zero-point energy spread as well as the additional broadening by the thermal population at  $T = 300$  K. Note that Eq. (2) is obtained by explicitly summing the Wigner distributions of the harmonic vibrational states [86] weighted with their thermal populations.

The equilibrium geometry and normal modes of *p*-aminophenol have been obtained with the GAUSSIAN16 program [87] at the density functional theory (DFT) level with the B3LYP functional and the *cc-pVTZ* basis set. The so obtained harmonic lowest frequency modes are out of plane bending of the OH and NH<sub>2</sub> groups at 151.12  $\text{cm}^{-1}$ , NH<sub>2</sub> torsion at 236.72  $\text{cm}^{-1}$ , and OH torsion at 293.88  $\text{cm}^{-1}$ , with thermal occupations >1% of the lowest 6, 4, and 4 vibra-

tional levels, respectively. The highest frequencies (smallest periods) correspond to the asymmetric N-H stretching mode with 3639.56  $\text{cm}^{-1}$  (9.17 fs) and the O-H stretching at 3823.92  $\text{cm}^{-1}$  (8.72 fs), respectively. However, the highest frequency mode that involves considerable motion of non-hydrogen atoms, and thus can be expected to affect the charge migration dynamics, is found at 1671.20  $\text{cm}^{-1}$  with a period of 19.96 fs. This gives us some confidence that neglecting the dynamic evolution of the nuclear wave packet is justified for the first 10 fs after the pump pulse. While anharmonic effects play an important role for modes below 800  $\text{cm}^{-1}$  [88], the higher (harmonic) mode frequencies obtained herein differ only by up to 5% from those in an experimental IR absorption spectrum [89]. Consequently, the harmonic approximation should suffice for our purpose of stochastically sampling molecular geometries from the Wigner distribution.

For five exemplary geometric parameters, the respective histograms obtained from the ensemble of 106 geometries are compared against those from a larger sample of  $10^4$  geometries in Figs. 2(b)–2(f). The visual comparison shows that the smaller ensemble of 106 geometries captures the main shape of the parameter distributions in all cases. In fact, the respective averages and standard deviations of both ensembles agree to a few percent, see Table I. Hence, the ensemble of 106 *p*-aminophenol geometries is sufficient for this study.

### C. Ionization amplitudes

To simulate the charge migration dynamics in *p*-aminophenol including the shot-to-shot variation and ground-state nuclear effects, the ionization amplitudes are explicitly evaluated for each pair of molecular geometry and pump pulse. To this end we employ the multicenter static exchange B-spline DFT approach [90,91] with the LB94 exchange-correlation functional to construct the molecular bound and continuum states with the correct asymptotic behavior [92]. This method has been amply and successfully used to evaluate photoionization cross sections for similarly sized molecules [93–99].

One obtains first the ground-state electron density of the neutral molecule in the basis of *TZP* Slater-type orbitals with the ADF package [100], from which the static exchange DFT Hamiltonian is evaluated in the B-spline basis. We chose herein a radial one-center expansion of B-splines spanning 20 a.u. with a maximum spacing of 0.2 a.u. originating at the center of the aromatic ring and angular functions constructed from spherical harmonics with up to  $l_{\text{OC}}^{\text{max}} = 31$ . This has been supplemented with small multicenter expansions at the atomic positions with  $l_{\text{MC,H}}^{\text{max}} = 1$  for the hydrogen and  $l_{\text{MC,OCN}}^{\text{max}} = 2$  for the other atoms to incorporate the flexibility to describe the electron density cusps at the atomic positions. To avoid numerical instabilities, their ranges have been decreased towards the origin from 0.8 a.u. for the outer H atoms, to 0.7 a.u. for the O, N, and C-attached H atoms, and 0.6 a.u. for the C atoms. The so-defined B-spline Hamiltonian is then diagonalized to obtain the bound Kohn-Sham (KS) molecular orbitals (MOs)  $|\phi_i\rangle$  and corresponding orbital energies  $\epsilon_i$ . Then,  $(l_{\text{OC}}^{\text{max}} + 1)^2 = 1024$  degenerate continuum MOs  $|\phi_L(\epsilon)\rangle$  are obtained for 36 equidistant kinetic energies  $\epsilon$  from 190.5 eV to 285.7 eV by diagonalizing the Hamiltonian

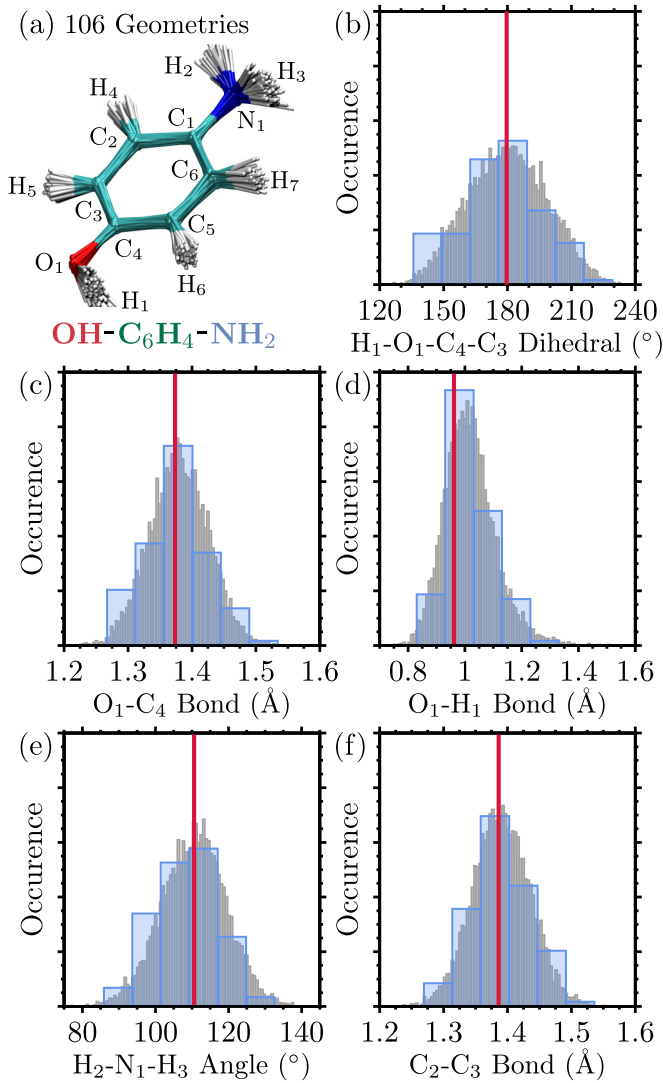


FIG. 2. (a) Overlay of 106 p-aminophenol geometries sampled at 300 K from the harmonic ground-state Wigner distribution. [(b)–(f)] Histograms of the denoted geometrical parameters over the ensemble of 106 geometries (blue) and a larger sample of  $10^4$  geometries (gray) with the corresponding equilibrium geometry values (red).

with the respectively appropriate boundary conditions [90,91]. These cover all kinetic energies resulting from ionization of p-aminophenol with all pulses employed herein.  $L = (l, m)$

TABLE I. Averages (standard deviations) of the geometric parameter distributions plotted in Figs. 2(b)–2(f) for the ensembles containing 106 and  $10^4$  molecular geometries, respectively.

Parameter	106 Geom.	$10^4$ Geom.
C <sub>2</sub> -C <sub>3</sub> (Å)	1.39 (0.05)	1.39 (0.04)
O <sub>1</sub> -C <sub>4</sub> (Å)	1.38 (0.05)	1.38 (0.05)
O <sub>1</sub> -H <sub>1</sub> (Å)	1.02 (0.08)	1.02 (0.09)
∠H <sub>2</sub> N <sub>1</sub> H <sub>3</sub> (°)	108.3 (8.6)	110.5 (8.8)
∠H <sub>1</sub> O <sub>1</sub> C <sub>4</sub> C <sub>3</sub> (°)	177.0 (19.0)	180.0 (18.4)

abbreviates pairs of angular momentum and magnetic quantum numbers.

Since orbital relaxation upon ionization and multi-reference effects are disregarded in this method, it yields only single MO ionized continuum states. Neglecting the orbital spins for the sake of clarity, they are constructed from the ground-state KS determinant  $|\Psi_0\rangle$  by promoting the  $i$ th bound MO to any of the continuum orbitals  $|\phi_L(\varepsilon)\rangle$ ,

$$|\Psi_{i,L}(\varepsilon)\rangle = \mathbf{a}_L^\dagger(\varepsilon) \underbrace{\mathbf{a}_i}_{|\Psi_0^+\rangle} |\Psi_0\rangle. \quad (3)$$

The so-defined one-hole continuum states have the energy  $\mathcal{E}_i + \varepsilon$ , where  $\mathcal{E}_i$  is the energy of the one-hole state of the remaining cation  $|\Psi_i^+\rangle$ . The broadband attosecond pump pulse creates a coherent superposition of these continuum states that evolves freely once the pulse has passed at time  $T$ ,

$$|\Psi(t)\rangle = \sum_{i,L} \int C_{i,L}^u(\varepsilon, T) |\Psi_{i,L}(\varepsilon)\rangle e^{-i(\mathcal{E}_i + \varepsilon)(T+t)} d\varepsilon. \quad (4)$$

Finally, the perturbative nature of the considered XFEL pulses permits to evaluate the photoionization amplitudes in first-order time-dependent perturbation theory and dipole approximation,

$$C_{i,L}^u(\varepsilon, T) = i \langle \phi_L(\varepsilon) | \mathbf{r} \cdot \mathbf{u} | \phi_i \rangle \int_0^T E(t) e^{i(\varepsilon_i + \varepsilon)t} dt, \quad (5)$$

with  $\mathbf{u}$  being the polarization direction of the field. Note that the ionization potentials of the  $i$ th MO  $\varepsilon_i = \mathcal{E}_i - \mathcal{E}_0$  are interpreted as the negative KS orbital energies  $\varepsilon_i = -\varepsilon_i$  according to the extended Koopman's theorem [101]. In practice, the time integral is replaced by the pulse's Fourier transform taken at the absorbed energy  $\int_0^T E(t) e^{i(\varepsilon_i + \varepsilon)t} dt \approx \sqrt{2\pi} \tilde{E}(T; \varepsilon_i + \varepsilon)^*$ . The transforms have been evaluated analytically for the 0.85 fs Gaussian pulse over a total duration of  $T = 2.375$  fs, corresponding its 0.999 percentile, and numerically up to 5.5 fs for the 100 XFEL pulses. Neglecting the tiny contributions of the XFEL pulses after 5.5 fs, see Sec. II A, overall affects the resulting Fourier transforms by no more than 2% of their maximum amplitude. The total number of ionization amplitudes,  $C_{i,L}^u(\varepsilon, T)$ , evaluated for each combination of XFEL pulse, molecular geometry, ionized valence MO, and continuum orbital is  $100 \times 106 \times 21 \times 1024 \approx 227 \times 10^6$  per polarization direction,  $x, y, z$ , and kinetic energy  $\varepsilon$ .

#### D. Charge migration dynamics

The charge migration is quantified in terms of the time dependent hole density induced by the sub-fs pulses in the p-aminophenol cation, which is the difference between the electron densities of the ground state and the coherent superposition of cationic states  $\rho_{\text{hole}}(\mathbf{r}, t) = \rho_0(\mathbf{r}) - \rho^+(\mathbf{r}, t)$  [4]. The hole densities have been evaluated following Refs. [70,102]. Therein, the continuum contributions to the hole dynamics have been found to vanish after about 0.5 fs [102]. So these are traced out of the complete wave packet in Eq. (4), reducing the complexity to a superposition of the  $N^+ = 21$  valence-MO-ionized bound states of the

p-aminophenol cation,

$$\hat{\rho}^+(t) = \sum_{i,j} \gamma_{ij} |\Psi_i^+\rangle \langle \Psi_j^+| e^{-i\varepsilon_{ij}(T+t)}. \quad (6)$$

To take into account the random orientation of the molecule with respect to the beam, the reduced density matrix has been averaged over the ionization amplitudes corresponding to the  $x$ ,  $y$ ,  $z$  polarization directions,

$$\gamma_{ij} = \frac{1}{3} \sum_{\alpha=x,y,z} \left[ \sum_L \int C_{i,L}^\alpha(\varepsilon, T) (C_{j,L}^\alpha(\varepsilon, T))^* d\varepsilon \right]. \quad (7)$$

It is normalized to  $\sum_i \gamma_{ii} = 1$  to establish the norm of the mixed quantum state  $\hat{\rho}^+(t)$  for each calculation regarding a pair of molecular geometry and sub-fs pulse. The corresponding spatial hole density is separated into a herein disregarded static part that integrates to unity, i.e., the hole's norm, and the dynamic portion [102] that is the focus of this paper,

$$\rho_{\text{hole}}^{\text{dyn}}(\mathbf{r}, t) = 2 \sum_{i < j} \Re \left[ \gamma_{ij} \phi_i^*(\mathbf{r}) \phi_j(\mathbf{r}) e^{-i\varepsilon_{ij}(T+t)} \right]. \quad (8)$$

It is a sum of oscillating contributions from all pairs of valence MOs  $i \neq j$ , for which the ionization potential (IP) difference  $\varepsilon_{ij}$  defines the respective frequencies, whereas amplitude and character are defined by  $\gamma_{ij}$  and the spatial product of the MOs, respectively. Note that the dynamic hole density integrates to zero, i.e. positive and negative lobes compensate each other, at all times.

To quantify the charge migration, localized dynamic hole charges were obtained by numerically integrating over volumes enclosing the  $A = \text{NH}_2$ ,  $\text{OH}$  molecular sites,  $Q_A(t) = \int_{V_A} \rho_{\text{hole}}^{\text{dyn}}(\mathbf{r}, t) d^3\mathbf{r}$ . The integration volumes were constructed from conjoined spheres with radii corresponding to 75% of the O-C and N-C distances on the oxygen (1.03 Å) and nitrogen atoms (1.05 Å), and the full H-O (0.96 Å) and H-N distances (1.01 Å) on the hydrogen atoms, respectively. On the  $\text{C}_6\text{H}_4$  ring it is calculated from the normalization of the dynamic hole density, which implies that all dynamic hole charges sum to zero,  $0 = Q_{\text{C}_6\text{H}_4}(t) + Q_{\text{NH}_2}(t) + Q_{\text{OH}}(t)$ . Positive (negative) values of these dynamic hole charges indicate electron deficiency (excess) at the corresponding sites of the p-aminophenol cation with respect to its static electron density.

To unravel the combined effect of the shot-to-shot variation and the ground-state nuclear wave function of p-aminophenol, the dynamic hole charges  $Q_A^{v,R}(t)$  obtained for each pair of XFEL pulse  $v$  and molecular geometric configuration  $\mathbf{R}$  are averaged in a two-step procedure. First, the average is taken for each pulse over the ensemble of  $N_R = 106$  geometries, resulting in pulse-specific averaged hole charges  $Q_A^v(t)$ . Second, these are averaged over the sample of  $N_p = 100$  XFEL pulses, using the pulse energies relative to their average as scaling factors,  $w_v = \mathcal{E}_v^{\text{pulse}} / \mathcal{E}_{\text{avg}}^{\text{pulse}}$ ,

$$Q_A(t) = \frac{1}{N_p} \sum_{v=1}^{N_p} w_v \left( \frac{1}{N_R} \sum_{\mathbf{R}} Q_A^{v,\mathbf{R}}(t) \right). \quad (9)$$

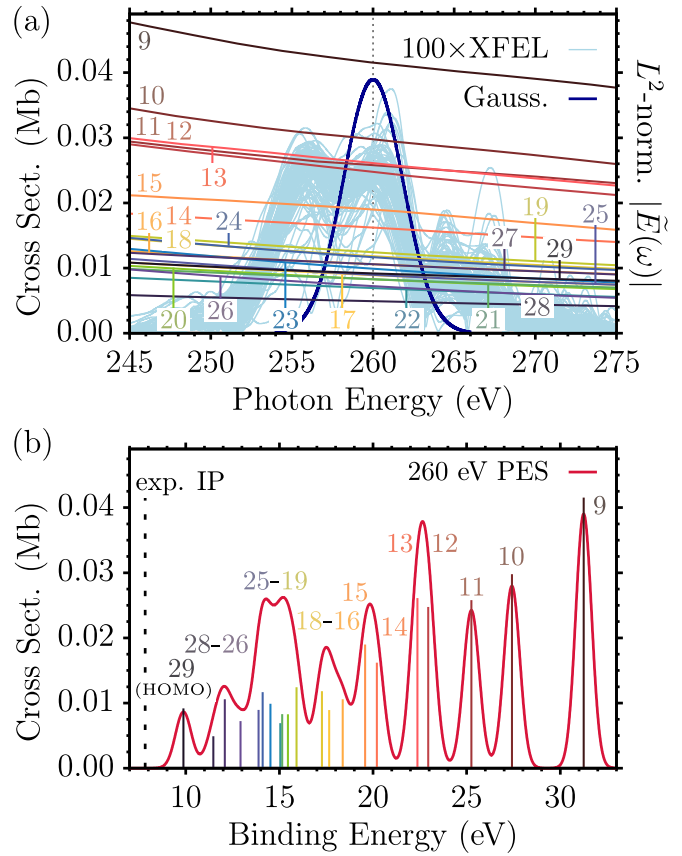


FIG. 3. (a) p-aminophenol equilibrium geometry MO ionization cross sections, in units of  $1 \text{ Mb} = 10^{-22} \text{ m}^2$ , overlaying the  $L^2$ -normalized  $|\tilde{E}(\omega)|$  spectra of the 100 XFEL pulses (blue) and the 0.85 fs 260 eV Gaussian pulse (dark blue). (b) PES for 260 eV cw-radiation. The cross section sticks of the 21 MO ionization channels, colors matching (a), have been broadened with a 1.0 eV Gaussian lineshape to obtain the continuous curve. The experimental lowest IP, 7.83 eV [103], is indicated.

This average incorporates the intensity fluctuation of the pulses relative to each other, see Fig. 1(b), since the degree of ionization obtained by each pulse is kept proportional to the energy deposited in the focal area, while exactly one electron per molecule is removed at the average pulse energy of 42.8  $\mu\text{J}$ . The scaling is necessary, since the effect of the intensity fluctuation has been previously removed by the normalization of the reduced density matrices, see discussion of Eq. (7).

### III. RESULTS AND DISCUSSION

To set the stage for analyzing the impact of the shot-to-shot variation and ground-state nuclear effects onto the charge migration in p-aminophenol, we first discuss its photoionization properties and electronic structure obtained with the static exchange B-spline DFT method. Figure 3(a) depicts the 21 valence MO photoionization cross sections for the equilibrium geometry overlaying the spectra of the 100 sub-fs XFEL pulses and the 0.85 fs 260 eV Gaussian pulse used for the charge migration calculation. Figure 3(b) contains the 260 eV continuous wave (cw) photoelectron spectrum (PES) at the pulses' carrier frequency. The sticks therein represent

a cut through the MO cross sections at 260 eV and sum to a total cross section of 0.313 Mb ( $10^{-22}$  m<sup>2</sup>). They have been broadened with a Gaussian FWHM of 1.0 eV to obtain a continuous curve in approximate correspondence to a synchrotron measurement of the valence PES with 260 eV radiation. Unfortunately, such a measurement could not be found in the available literature. Both panels show that despite the cross sections being largest for the inner valence orbitals 10,  $\sigma_{\text{NC}}$ , and 9,  $\sigma_{\text{OC}}$ , all MO ionization channels contribute to the spectrum and none of them can be disregarded from the electronic wave packet, Eq. (4). Remarkably, the lowest experimental IP of 7.83 eV [103], indicated in panel (b), lies around 2 eV below our theoretical prediction, which can be attributed to the LB94 functional leading to an overestimation of the outer valence MO IPs. This characteristic has also been found in previous studies [68–70,102]. Since the cross sections are rather flat at these high energies, however, we do not expect the photoionization amplitudes to be notably affected by this discrepancy. The respective PES obtained with the Gaussian and XFEL sub-fs pulses are presented in the Appendix.

The charge motion initiated in p-aminophenol by ionization with the 0.85 fs 260 eV Gaussian pulse is illustrated in Fig. 4(a), depicting snapshots of the dynamic hole density, Eq. (8), at times of prominent charge displacement. Additionally indicated are the integration volumes that have been used to obtain the localized dynamic hole charges  $Q_A(t)$  at the OH, NH<sub>2</sub>, and C<sub>6</sub>H<sub>4</sub> sites as detailed in Sec. IID. Their temporal evolution is plotted in Fig. 4(b), while Fig. 4(c) contains the corresponding infinite-time Fourier transformations broadened with a Gaussian FWHM of 0.08 eV to obtain continuous curves. At  $t = 0$  fs after the Gaussian pulse, our simulations predict a respective surplus and deficiency of electronic charge on the OH and NH<sub>2</sub> groups and an approximately zero net charge on the C<sub>6</sub>H<sub>4</sub> ring, with respect to the static electron density in the cation. From this point, the charge motion evolves on the full molecule with periods of 1.5 fs–2.5 fs, involving mainly the OH group and the C<sub>6</sub>H<sub>4</sub> ring, while the NH<sub>2</sub> group participates to a lesser extent. Therein, the dynamic hole charges never exceed a few percent of the total hole, in line with previous works [69,102].

To illustrate the effect of the shot-to-shot variation in the time and frequency domain Figs. 4(b) and 4(c), respectively, also depict the pulse-energy-scaled averages obtained for the 100 XFEL pulses in the equilibrium geometry. The timescale of the pulse-averaged dynamics has been shifted by 0.31 fs to compensate the later entry into the free evolution due to the broader temporal envelope of the XFEL pulses, see Fig. 1. With this alignment, the feature positions and characteristics in the pulse-averaged time evolution of the hole charges at all sites barely deviate from those obtained with the Gaussian pulse. The main effect of the shot-to-shot variation and the overall different spectral characteristics of the XFEL pulses is thus the reduction of the hole charge amplitudes by up to 35% with respect to the Gaussian pulse results. The Fourier transforms in panel (c) reveal multiple frequency contributions at each molecular site, with the most prominent ones, labeled 1–6, corresponding to frequencies (periods) in the range of 0.65 eV (6.4 fs) to 3.1 eV (1.3 fs). The amplitude reduction by the shot-to-shot variation translates to the frequency domain as well, however, not evenly. The low frequency components

1 and 2 (<1 eV) are less affected than 3–6 at higher frequencies, which appear to be more susceptible to the shot-to-shot variation and spectra of the XFEL pulses.

The isolated effect of the ground-state nuclear wave function, represented by the ensemble of 106 nuclear geometries, see Fig. 2, on the dynamic hole charges obtained with the Gaussian pulse is shown in Figs. 4(d) and 4(e). Therein, the fluctuations of the temporal dynamic hole charges are damped by about 85% within the first 3 fs. During this time, the dynamic hole charges approximately correspond to the progressively damped equilibrium-geometry result in panel (b). Beyond 3 fs, however, the oscillations reach still up to about 20% of their maximum amplitude, in approximate agreement with a previous study [72]. This is due to the fact that all quantities defining the dynamic hole density in Eq. (8), i.e., the oscillation frequencies, ionization amplitudes, and spatial orbital functions depend on the molecular geometry. The frequency analysis of the geometry averaged dynamics in panel (e) reflects this effect. It comprises a prominent low-frequency band until 2.5 eV (1.7 fs) and a less intense band until 4.3 eV (1.0 fs) instead of the respective sharp features obtained for the equilibrium geometry with the shot-to-shot variation in panel (c).

Finally, the combined effect of the XFEL shot-to-shot variation and the ground-state nuclear wave function on the hole charges is presented in Figs. 4(f) and 4(g). Therein plotted are the total averages over the results for 100 XFEL pulses, each of which averages over the ensemble of 106 molecular geometries, see Eq. (9). In addition, the 95% confidence intervals for the outer average over the XFEL pulses illustrate the stochastic uncertainty derived from the shot-to-shot variation, see Fig. 1. In the time and frequency domains they respectively span at maximum  $\pm 10\%$  and  $\pm 20\%$  around the average values, demonstrating that the here employed ensemble of XFEL pulses is large enough to yield meaningful results.

Similarly to our initial results for the equilibrium geometry of p-aminophenol, the additional inclusion of the XFEL shot-to-shot variation and pulse spectra on top of the ground-state nuclear effects leads to a reduction of the maximum hole charge amplitudes in the time and frequency domains by up to 30% in comparison to the geometry-averaged Gaussian pulse results in Figs. 4(d) and 4(e). The characteristics of the dynamics, however, is not altered significantly, although some features appear less prominent. In particular, the progressive damping of the charge dynamics due to the ground-state nuclear effects is not affected by the shot-to-shot variation in the present ensemble of 100 XFEL pulses.

The main cause for the dephasing lies in the fluctuation of the prominent oscillation frequencies defined by the orbital IPs,  $\varepsilon_{ij} = \varepsilon_i - \varepsilon_j$ , with the geometry. This is illustrated in Fig. 5, which depicts histograms of the oscillating frequencies of the four dominant terms in the OH dynamic hole charge that have been obtained for the 106 geometries combined with (i) the Gaussian pulse and (ii) the ensemble of 100 pulses. As can be seen, the inclusion of the shot-to-shot variation on top of the geometry ensemble in (ii) does not significantly broaden the distribution of the four leading oscillating frequencies obtained with just the nuclear ground-state effects in (i). Hence it does not considerably accelerate the dephasing of the dynamics, even though it shifts the respective average frequencies to

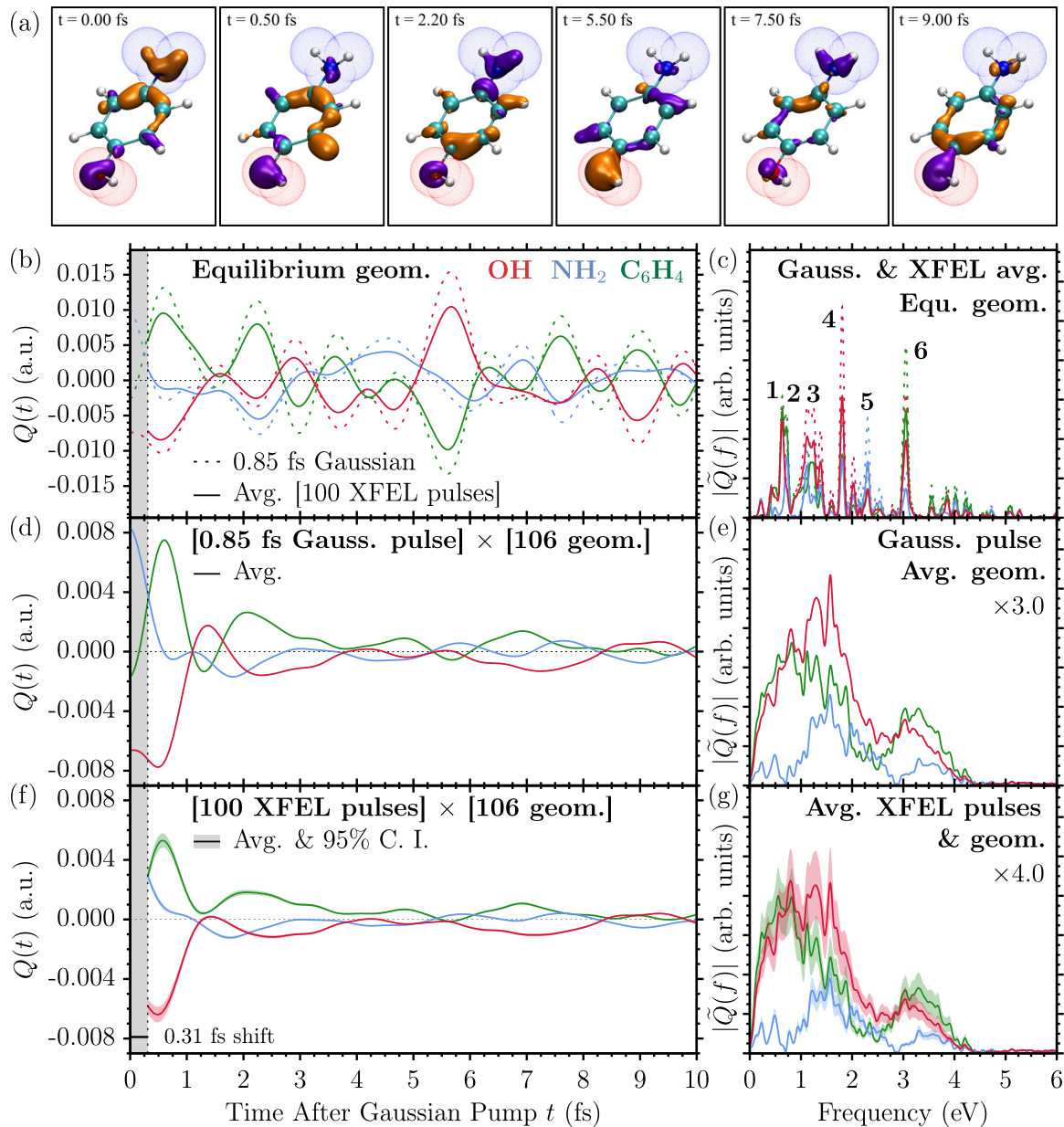


FIG. 4. (a) Snapshots of prominent hole density dynamics, Eq. (8), induced by ionization with the 0.85 fs 260 eV Gaussian pulse in the equilibrium geometry of p-aminophenol. Violet (orange) lobes correspond to negative (positive) hole density with isovalue 0.0003. The integration volumes to obtain the hole charges at the OH and NH<sub>2</sub> sites are indicated in red and blue. (b) Evolution of the hole charges  $Q(t)$ , at the OH (red), NH<sub>2</sub> (blue), and C<sub>6</sub>H<sub>4</sub> (green) sites in the equilibrium geometry. Gaussian pulse results (dashed) are compared against averages over the 100 XFEL pulses (solid). The pulse-averaged dynamics have been shifted by 0.31 fs to align with the Gaussian pulse timescale, see Fig. 1. (c) Absolute values of the corresponding Fourier transforms  $|\tilde{Q}(f)|$ . [(d), (e)] Same as (b) and (c) but now showing the respective averages over 106 molecular geometries for the Gaussian pulse. [(f), (g)] Respective results averaged over the 100 XFEL pulses and, for each pulse, over the ensemble of geometries. The corresponding 95% confidence intervals (shaded) are depicted as well. The scaling factors in panels (e) and (g) have been chosen such that the vertical range is the same as in (c).

slightly lower values. It should, however, be noted that these findings hold only for pulse ensembles that do not encompass a considerably stronger shot-to-shot fluctuation than the one employed herein.

#### IV. CONCLUSIONS AND OUTLOOK

We have shown that charge migration induced by 260 eV sub-fs XFEL pulses in p-aminophenol is not significantly

affected by their intrinsic shot-to-shot variation, which we represented by an ensemble of 100 pulses obtained from start-to-end simulations of the x-ray laser-enhanced attosecond pulse generation procedure implemented at the LCLS [63]. The obtained amplitude reduction of the charge fluctuations due to this effect is far less important than that due to the natural geometrical variation of the molecule associated with its initial-state nuclear wave function. The latter effect significantly damps the generated charge dynamics beyond 3 fs.

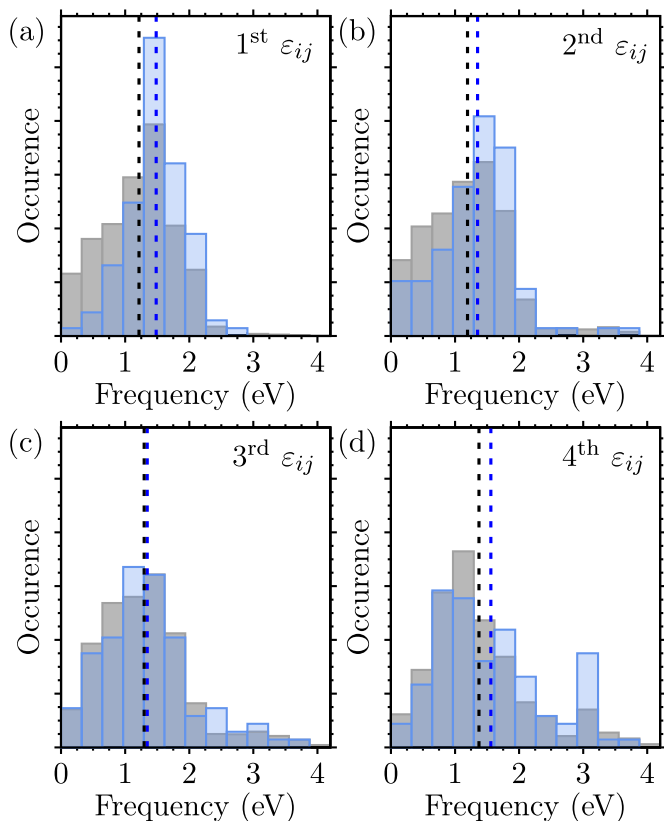


FIG. 5. [(a)–(d)] Histograms of the oscillation frequencies  $\varepsilon_{ij}$  with the 1st–4th largest weight in the Fourier analysis of the OH hole charge dynamics. The results for the 0.85 fs 260 eV Gaussian pulse and the 106-geometry ensemble, see Fig. 4(e), are depicted in blue; gray denotes those obtained for the combination of the 100 XFEL pulses and the 106 molecular geometries, see Fig. 4(g). The blue and black dashed lines denote the respective averages.

These results suggest that as long as the shot-to-shot variation is not significantly stronger than in this work, attosecond soft x-ray spectroscopies at XFELs, as, e.g., those already available at the LCLS [63], can be reliably used to investigate pristine charge dynamics at its early stages. Further, this result means that with high-repetition rate XFELs charge migration can be rapidly measured at their full rate without the need to measure and detect only the data for a minority of pulses.

#### ACKNOWLEDGMENTS

We gratefully acknowledge financial support from the FULMATEN project (Ref. Y2018 NMT-5028) from the Comunidad de Madrid and the European Union, the Ministerio de Ciencia e Innovación (MICINN) projects PID2019-105458RB-I00, the Severo Ochoa Programme for Centres of Excellence in R&D (CEX2020-001039-S), and the María de Maeztu Programme for Units of Excellence in R&D (CEX2018-000805-M). We thank the Centro de Computación Científica (CCC) of the Universidad Autónoma de Madrid, and the Barcelona supercomputing center (BSC) for the granted CPU time. Further support of this work has been received from the U.S. Department of Energy (DOE) Contract No. DE-AC02-76SF00515 and the DOE

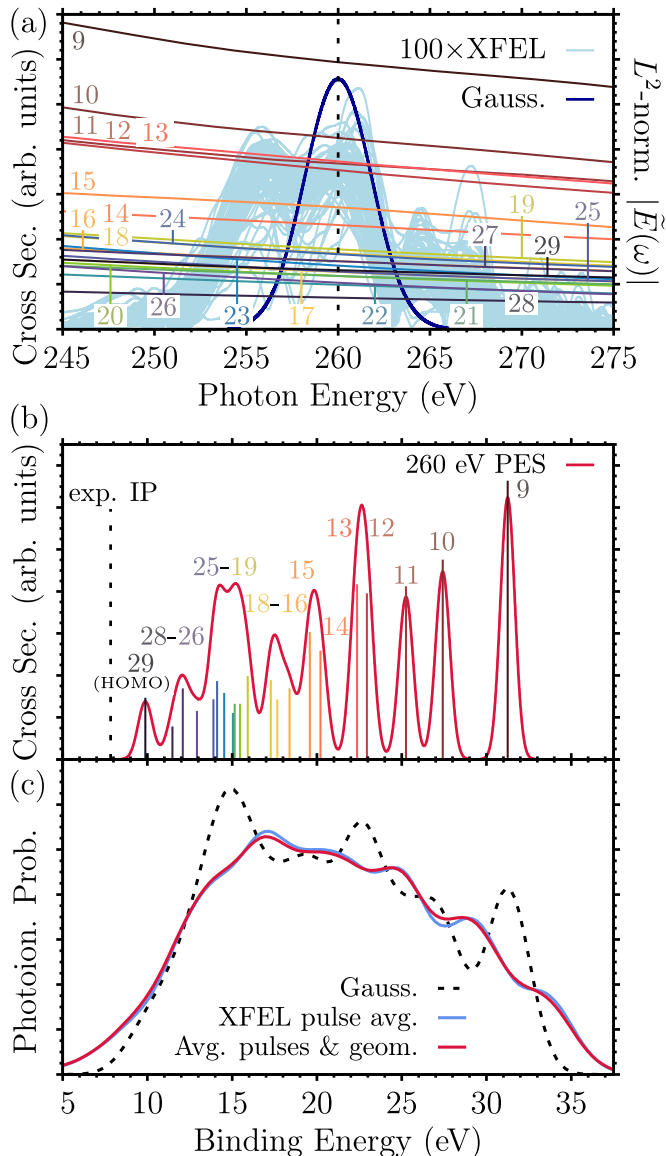


FIG. 6. (a) p-aminophenol equilibrium geometry MO ionization cross sections overlaying the  $|\tilde{E}(\omega)|$  spectra of the 100 XFEL pulses (blue) and the 0.85 fs 260 eV Gaussian pulse (dark blue). (b) PES for 260 eV cw-radiation. The stick intensities of the 21 MO ionization channels, colors matching (a), have been broadened with a 1.0 eV Gaussian lineshape. The experimental lowest IP, 7.83 eV [103], is indicated. (c) Equilibrium geometry PES obtained with the 0.85 fs 260 eV Gaussian pulse (dashed); average PES over 100 XFEL pulses for the equilibrium geometry (blue) and additionally averaged over the 106 geometries for each pulse (red). Linear scales are used in all panels.

Basic Energy Sciences Accelerator and Detector Research program. Z.G. acknowledges the support from the Robert H. Siemann Graduate Fellowship in Physics. The work of J.P.C. and T.D. was supported by the U.S. DOE, Office of Science, Basic Energy Sciences, Chemical Sciences, Geosciences, and Biosciences Division. P.W. was supported by the Linac Coherent Light Source (LCLS), SLAC National Accelerator Laboratory, which is supported by the U.S. Department of Energy, Office of Science, Office of Basic



Energy Sciences under Contract No. DE-AC02-76SF00515. J.P.M. was supported by the U.K. Engineering and Physical Sciences Research Council Grants No. EP/R019509/1 and No. EP/T006943/1. A.P. was supported by grants ref. 2021-5A/IND-20959 (Comunidad Madrid) and ref. PID2021-126560NB-I00 (MCIU/AEI/FEDER, UE).

#### APPENDIX: ATTOSECOND-PULSE PHOTOIONIZATION SPECTRA

Figures 6(a) and 6(b) are reproduced from Fig. 3 in the main text to facilitate the discussion of the p-aminophenol PES obtained with the sub-fs pulses depicted in Fig. 6(c). The latter contains the equilibrium geometry PES induced by the 0.85 fs 260 eV Gaussian pulse and, respectively, averaged over the 100 XFEL pulses to account for the shot-to-shot variation and realistic pulse envelopes. Further, the PES including the effect of the initial nuclear wave function by averaging over the 106 molecular geometries in addition to the shot-to-shot variation is shown as well. The PES for each pulse and molecular geometry have been obtained as the photoionization probability per photoelectron kinetic energy by summing the respective squared photoionization amplitudes, see Eq. (5) of the main text, over the continuum angular parts  $L = (l, m)$  and the ionized valence MOs  $i$ ,

$$P(\varepsilon) = \frac{1}{3} \sum_{\alpha=x,y,z} \sum_{i,L} |C_{i,L}^{\alpha}(\varepsilon, T)|^2. \quad (\text{A1})$$

Averaging over the polarization directions is carried out to account for the random orientation of the molecule with respect to the polarization of the ionizing pulses. The resulting PES have then been transformed to the binding energy scale by subtracting the kinetic energy from the respectively different central photon energies of each pulse  $\mathcal{E}_B = \omega_{\nu} - \varepsilon$ . Subse-

quently, the averages over the XFEL pulses and geometries have been evaluated evenly over the binding-energy-scale PES. In that way, the intensity fluctuations of the pulses, depicted in Fig. 1 of the main text, are incorporated via the photoionization amplitudes. Finally, the spectra shown in Fig. 6(c) have been normalized to the area under their respective curves.

In the shot-to-shot averaged PES, the local maxima appear displaced by about  $\pm 2$  eV with respect to those in the Gaussian pulse PES that are aligned perfectly with the main features in the 260 eV cw PES in panel (b). This can be attributed to the different sub-fs pulses' spectra, which are imprinted into the lineshape of each single-MO ionization feature via the respective photoionization amplitudes. In the continuous wave case, these appear as infinitely narrow sticks at the MO IPs. However, the 0.85 fs 260 eV Gaussian and XFEL pulses have spectra of nonzero width, see panel (a), respectively corresponding to a Gaussian shape with a FWHM of 4.3 eV and rough double-peak structures having an overall FWHM of  $\approx 8.0$  eV. The two local maxima of the latter appear displaced by about  $\pm 2$  eV around the respective central photon energies of the pulses. Upon summation of the single-MO ionization features to the total PES, depicted in panel (c), this results in the observed different placement of the local maxima in the Gaussian pulse and shot-to-shot averaged PES curves, respectively.

Taking into account the width of the initial nuclear wave function by averaging over the ensemble of 106 geometries, see Sec. II B of the main text, on top of the XFEL shot-to-shot variation leads to an almost indistinguishable PES in comparison to only including the average over the XFEL pulses. This shows that the variation of the static PES due to the width of the nuclear wave function at  $T = 300$  K is in this case much smaller than the effect of the sub-fs pulses' spectral shape.

- 
- [1] R. Weinkauff, P. Schanen, D. Yang, S. Soukara, and E. W. Schlag, Elementary processes in peptides: Electron mobility and dissociation in peptide cations in the gas phase, *J. Phys. Chem.* **99**, 11255 (1995).
- [2] R. Weinkauff, P. Schanen, A. Metsala, E. W. Schlag, M. Bürgle, and H. Kessler, Highly efficient charge transfer in peptide cations in the gas phase: Threshold effects and mechanism, *J. Phys. Chem.* **100**, 18567 (1996).
- [3] F. Remacle, R. D. Levine, and M. A. Ratner, Charge directed reactivity: A simple electronic model, exhibiting site selectivity, for the dissociation of ions, *Chem. Phys. Lett.* **285**, 25 (1998).
- [4] L. S. Cederbaum and J. Zobeley, Ultrafast charge migration by electron correlation, *Chem. Phys. Lett.* **307**, 205 (1999).
- [5] T. Renger, V. May, and O. Kühn, Ultrafast excitation energy transfer dynamics in photosynthetic pigment-protein complexes, *Phys. Rep.* **343**, 137 (2001).
- [6] S. K. Kurinec, ed., *Emerging Photovoltaic Materials: Silicon & Beyond* (Scrivener Publishing LLC, Beverly, MA, 2019).
- [7] H. Chen and J. Fraser Stoddart, From molecular to supramolecular electronics, *Nat. Rev. Mater.* **6**, 804 (2021).
- [8] E. Alizadeh, T. M. Orlando, and L. Sanche, Biomolecular damage induced by ionizing radiation: The direct and indirect effects of low-energy electrons on DNA, *Annu. Rev. Phys. Chem.* **66**, 379 (2015).
- [9] S. Weber, Light-driven enzymatic catalysis of DNA repair: A review of recent biophysical studies on photolyase, *Biochim. Biophys. Acta* **1707**, 1 (2005).
- [10] M. F. Kling and M. J. J. Vrakking, Attosecond electron dynamics, *Annu. Rev. Phys. Chem.* **59**, 463 (2008).
- [11] F. Krausz and M. Ivanov, Attosecond physics, *Rev. Mod. Phys.* **81**, 163 (2009).
- [12] S. R. Leone, C. W. McCurdy, J. Burgdörfer, L. S. Cederbaum, Z. Chang, N. Dudovich, J. Feist, C. H. Greene, M. Ivanov, R. Kienberger *et al.*, What will it take to observe processes in 'real time'?, *Nat. Photonics* **8**, 162 (2014).
- [13] F. Calegari, G. Sansone, S. Stagira, C. Vozzi, and M. Nisoli, Advances in attosecond science, *J. Phys. B: At. Mol. Opt. Phys.* **49**, 062001 (2016).
- [14] F. Calegari, D. Ayuso, A. Trabattini, L. Belshaw, S. De Camillis, S. Anumula, F. Frassetto, L. Poletto, A. Palacios, P. Declava *et al.*, Ultrafast electron dynamics in phenylalanine initiated by attosecond pulses, *Science* **346**, 336 (2014).
- [15] F. Lépine, M. Y. Ivanov, and M. J. J. Vrakking, Attosecond molecular dynamics: Fact or fiction?, *Nat. Photonics* **8**, 195 (2014).

- [16] N. V. Golubev and A. I. Kuleff, Control of charge migration in molecules by ultrashort laser pulses, *Phys. Rev. A* **91**, 051401(R) (2015).
- [17] M. Nisoli, P. Decleva, F. Calegari, A. Palacios, and F. Martín, Attosecond electron dynamics in molecules, *Chem. Rev.* **117**, 10760 (2017).
- [18] A. Palacios and F. Martín, The quantum chemistry of attosecond molecular science, *WIREs Comput. Mol. Sci.* **10**, e1430 (2020).
- [19] I. C. D. Merritt, D. Jacquemin, and M. Vacher, Attochemistry: Is controlling electrons the future of photochemistry?, *J. Phys. Chem. Lett.* **12**, 8404 (2021).
- [20] P. M. Paul, E. S. Toma, P. Breger, G. Mullot, F. Augé, P. Balcou, H. G. Muller, and P. Agostini, Observation of a train of attosecond pulses from high harmonic generation, *Science* **292**, 1689 (2001).
- [21] M. Hentschel, R. Kienberger, C. Spielmann, G. A. Reider, N. Milosevic, T. Brabec, P. Corkum, U. Heinzmann, M. Drescher, and F. Krausz, Attosecond metrology, *Nature (London)* **414**, 509 (2001).
- [22] F. Frank, C. Arrell, T. Witting, W. A. Okell, J. McKenna, J. S. Robinson, C. A. Haworth, D. Austin, H. Teng, I. A. Walmsley *et al.*, Invited review article: Technology for attosecond science, *Rev. Sci. Instrum.* **83**, 071101 (2012).
- [23] J. Li, J. Lu, A. Chew, S. Han, J. Li, Y. Wu, H. Wang, S. Ghimire, and Z. Chang, Attosecond science based on high harmonic generation from gases and solids, *Nat. Commun.* **11**, 2748 (2020).
- [24] S. Baker, J. S. Robinson, C. A. Haworth, H. Teng, R. A. Smith, C. C. Chirila, M. Lein, J. W. G. Tisch, and J. P. Marangos, Probing proton dynamics in molecules on an attosecond time scale, *Science* **312**, 424 (2006).
- [25] M. F. Kling, C. Siedschlag, A. J. Verhoef, J. I. Khan, M. Schultze, T. Uphues, Y. Ni, M. Uiberacker, M. Drescher, F. Krausz *et al.*, Control of electron localization in molecular dissociation, *Science* **312**, 246 (2006).
- [26] G. Sansone, F. Kelkensberg, J. F. Pérez-Torres, F. Morales, M. F. Kling, W. Siu, O. Ghafur, P. Johnsson, M. Swoboda, E. Benedetti *et al.*, Electron localization following attosecond molecular photoionization, *Nature (London)* **465**, 763 (2010).
- [27] O. Smirnova, Y. Mairesse, S. Patchkovskii, N. Dudovich, D. Villeneuve, P. Corkum, and M. Y. Ivanov, High harmonic interferometry of multi-electron dynamics in molecules, *Nature (London)* **460**, 972 (2009).
- [28] C. Neidel, J. Klei, C.-H. Yang, A. Rouzée, M. J. J. Vrakking, K. Klünder, M. Miranda, C. L. Arnold, T. Fordell, A. L'Huillier, M. Gisselbrecht, P. Johnsson, M. P. Dinh, E. Suraud, P.-G. Reinhard, V. Despré, M. A. L. Marques, and F. Lépine, Probing Time-Dependent Molecular Dipoles on the Attosecond Time Scale, *Phys. Rev. Lett.* **111**, 033001 (2013).
- [29] P. M. Kraus, B. Mignolet, D. Baykusheva, A. Rupenyan, L. Horny, E. F. Penka, G. Grassi, O. I. Tolstikhin, J. Schneider, F. Jensen *et al.*, Measurement and laser control of attosecond charge migration in ionized iodoacetylene, *Science* **350**, 790 (2015).
- [30] S. Haessler, J. Caillat, W. Boutu, C. Giovanetti-Teixeira, T. Ruchon, T. Auguste, Z. Diveki, P. Breger, A. Maquet, B. Carré *et al.*, Attosecond imaging of molecular electronic wavepackets, *Nat. Phys.* **6**, 200 (2010).
- [31] T. Okino, Y. Furukawa, Y. Nabekawa, S. Miyabe, A. Amani Eilanlou, E. J. Takahashi, K. Yamanouchi, and K. Midorikawa, Direct observation of an attosecond electron wave packet in a nitrogen molecule, *Sci. Adv.* **1**, e1500356 (2015).
- [32] F. Kelkensberg, W. Siu, J. F. Pérez-Torres, F. Morales, G. Gademann, A. Rouzée, P. Johnsson, M. Lucchini, F. Calegari, J. L. Sanz-Vicario, F. Martín, and M. J. J. Vrakking, Attosecond Control in Photoionization of Hydrogen Molecules, *Phys. Rev. Lett.* **107**, 043002 (2011).
- [33] P. Ranitovic, C. W. Hogle, P. Rivière, A. Palacios, X.-M. Tong, N. Toshima, A. González-Castrillo, L. Martín, F. Martín, M. M. Murnane *et al.*, Attosecond vacuum UV coherent control of molecular dynamics, *Proc. Natl. Acad. Sci.* **111**, 912 (2014).
- [34] I. Znakovskaya, P. von den Hoff, S. Zherebtsov, A. Wirth, O. Herrwerth, M. J. J. Vrakking, R. de Vivie-Riedle, and M. F. Kling, Attosecond Control of Electron Dynamics in Carbon Monoxide, *Phys. Rev. Lett.* **103**, 103002 (2009).
- [35] W. Siu, F. Kelkensberg, G. Gademann, A. Rouzée, P. Johnsson, D. Dowek, M. Lucchini, F. Calegari, U. De Giovannini, A. Rubio *et al.*, Attosecond control of dissociative ionization of O<sub>2</sub> molecules, *Phys. Rev. A* **84**, 063412 (2011).
- [36] A. Alnaser, M. Kübel, R. Siemerling, B. Bergues, N. G. Kling, K. Betsch, Y. Deng, J. Schmidt, Z. Alahmed, A. Azzeer *et al.*, Subfemtosecond steering of hydrocarbon deprotonation through superposition of vibrational modes, *Nat. Commun.* **5**, 3800 (2014).
- [37] M. Lewenstein, P. Balcou, M. Y. Ivanov, A. L'Huillier, and P. B. Corkum, Theory of high-harmonic generation by low-frequency laser fields, *Phys. Rev. A* **49**, 2117 (1994).
- [38] P. A. Carpeggiani, P. Tzallas, A. Palacios, D. Gray, F. Martín, and D. Charalambidis, Disclosing intrinsic molecular dynamics on the 1-fs scale through extreme-ultraviolet pump-probe measurements, *Phys. Rev. A* **89**, 023420 (2014).
- [39] D. Fabris, T. Witting, W. A. Okell, D. J. Walke, P. Matia-Hernando, J. Henkel, T. R. Barillot, M. Lein, J. P. Marangos, and J. W. G. Tisch, Synchronized pulses generated at 20 eV and 90 eV for attosecond pump-probe experiments, *Nat. Photonics* **9**, 383 (2015).
- [40] I. Makos, I. Orfanos, A. Nayak, J. Peschel, B. Major, I. Lontos, E. Skantzakis, N. Papadakis, C. Kalpouzos, M. Dumergue *et al.*, A 10-gigawatt attosecond source for nonlinear XUV optics and XUV-pump-XUV-probe studies, *Sci. Rep.* **10**, 3759 (2020).
- [41] I. V. Schweigert and S. Mukamel, Probing valence electronic wave-packet dynamics by all x-ray stimulated Raman spectroscopy: A simulation study, *Phys. Rev. A* **76**, 012504 (2007).
- [42] S. Mukamel, D. Healton, Y. Zhang, and J. D. Biggs, Multidimensional attosecond resonant x-ray spectroscopy of molecules: Lessons from the optical regime, *Annu. Rev. Phys. Chem.* **64**, 101 (2013).
- [43] N. Huse, T. K. Kim, L. Jamula, J. K. McCusker, F. M. F. de Groot, and R. W. Schoenlein, Photo-induced spin-state conversion in solvated transition metal complexes probed via time-resolved soft x-ray spectroscopy, *J. Am. Chem. Soc.* **132**, 6809 (2010).
- [44] Y. Zhang, W. Hua, K. Bennett, and S. Mukamel, Topics in current chemistry, in *Density-Functional Methods for Excited States*, edited by N. Ferré, M. Filatov, and M. Huix-Rotllant (Springer, Cham, 2014), Vol. 368, pp. 273–345.

- [45] A. R. Attar, A. Bhattacharjee, C. D. Pemmaraju, K. Schnorr, K. D. Closser, D. Prendergast, and S. R. Leone, Femtosecond x-ray spectroscopy of an electrocyclic ring-opening reaction, *Science* **356**, 54 (2017).
- [46] T. J. A. Wolf, R. H. Myhre, J. P. Cryan, S. Coriani, R. J. Squibb, A. Battistoni, N. Berrah, C. Bostedt, P. Bucksbaum, G. Coslovich *et al.*, Probing ultrafast  $\pi\pi^*/n\pi^*$  internal conversion in organic chromophores via K-edge resonant absorption, *Nat. Commun.* **8**, 29 (2017).
- [47] Y. Pertot, C. Schmidt, M. Matthews, A. Chauvet, M. Huppert, V. Svoboda, A. von Conta, A. Tehlar, D. Baykusheva, J.-P. Wolf *et al.*, Time-resolved x-ray absorption spectroscopy with a water window high-harmonic source, *Science* **355**, 264 (2017).
- [48] S. Oberli, J. González-Vázquez, E. Rodríguez-Perelló, M. Sodupe, F. Martín, and A. Picón, Site-selective-induced isomerization of formamide, *Phys. Chem. Chem. Phys.* **21**, 25626 (2019).
- [49] J. T. O'Neal, E. G. Champenois, S. Oberli, R. Obaid, A. Al-Haddad, J. Barnard, N. Berrah, R. Coffee, J. Duris, G. Galinis *et al.*, Electronic Population Transfer via Impulsive Stimulated X-Ray Raman Scattering with Attosecond Soft-X-Ray Pulses, *Phys. Rev. Lett.* **125**, 073203 (2020).
- [50] S. Li, T. Driver, O. Alexander, B. Cooper, D. Garratt, A. Marinelli, J. P. Cryan, and J. P. Marangos, Time-resolved pump-probe spectroscopy with spectral domain ghost imaging, *Faraday Discuss.* **228**, 488 (2021).
- [51] S. M. Teichmann, F. Silva, S. L. Cousin, M. Hemmer, and J. Biegert, 0.5-keV soft x-ray attosecond continua, *Nat. Commun.* **7**, 11493 (2016).
- [52] T. Gaumnitz, A. Jain, Y. Pertot, M. Huppert, I. Jordan, F. Ardana-Lamas, and H. J. Wörner, Streaking of 43-attosecond soft-x-ray pulses generated by a passively CEP-stable mid-infrared driver, *Opt. Express* **25**, 27506 (2017).
- [53] J. Li, X. Ren, Y. Yin, K. Zhao, A. Chew, Y. Cheng, E. Cunningham, Y. Wang, S. Hu, Y. Wu *et al.*, 53-attosecond x-ray pulses reach the carbon K-edge, *Nat. Commun.* **8**, 186 (2017).
- [54] S. L. Cousin, N. Di Palo, B. Buades, S. M. Teichmann, M. Reduzzi, M. Devetta, A. Kheifets, G. Sansone, and J. Biegert, Attosecond Streaking in the Water Window: A New Regime of Attosecond Pulse Characterization, *Phys. Rev. X* **7**, 041030 (2017).
- [55] A. S. Johnson, D. R. Austin, D. A. Wood, C. Brahm, A. Gregory, K. B. Holzner, S. Jarosch, E. W. Larsen, S. Parker, C. S. Strüber *et al.*, High-flux soft x-ray harmonic generation from ionization-shaped few-cycle laser pulses, *Sci. Adv.* **4**, eaar3761 (2018).
- [56] B. W. J. McNeil and N. R. Thompson, X-ray free-electron lasers, *Nat. Photonics* **4**, 814 (2010).
- [57] W. Ackermann, G. Asova, V. Ayvazyan, A. Azima, N. Baboi, J. Bähr, V. Balandin, B. Beutner, A. Brandt, A. Bolzmann *et al.*, Operation of a free-electron laser from the extreme ultraviolet to the water window, *Nat. Photonics* **1**, 336 (2007).
- [58] P. Emma, R. Akre, J. Arthur, R. Bionta, C. Bostedt, J. Bozek, A. Brachmann, P. Bucksbaum, R. Coffee, F.-J. Decker *et al.*, First lasing and operation of an ångström-wavelength free-electron laser, *Nat. Photonics* **4**, 641 (2010).
- [59] M. Altarelli, The European x-ray free-electron laser facility in Hamburg, *Nucl. Instrum. Methods Phys. Res., Sect. B* **269**, 2845 (2011).
- [60] T. Ishikawa, H. Aoyagi, T. Asaka, Y. Asano, N. Azumi, T. Bizen, H. Ego, K. Fukami, T. Fukui, Y. Furukawa *et al.*, A compact x-ray free-electron laser emitting in the sub-ångström region, *Nat. Photonics* **6**, 540 (2012).
- [61] H.-S. Kang, C.-K. Min, H. Heo, C. Kim, H. Yang, G. Kim, I. Nam, S. Y. Baek, H.-J. Choi, G. Mun *et al.*, Hard x-ray free-electron laser with femtosecond-scale timing jitter, *Nat. Photonics* **11**, 708 (2017).
- [62] T. Barillot, O. Alexander, B. Cooper, T. Driver, D. Garratt, S. Li, A. Al Haddad, A. Sanchez-Gonzalez, M. Agåker, C. Arrell *et al.*, Correlation-Driven Transient Hole Dynamics Resolved in Space and Time in the Isopropanol Molecule, *Phys. Rev. X* **11**, 031048 (2021).
- [63] J. Duris, S. Li, T. Driver, E. G. Champenois, J. P. MacArthur, A. A. Lutman, Z. Zhang, P. Rosenberger, J. W. Aldrich, R. Coffee *et al.*, Tunable isolated attosecond X-ray pulses with gigawatt peak power from a free-electron laser, *Nat. Photonics* **14**, 30 (2020).
- [64] A. A. Lutman, R. Coffee, Y. Ding, Z. Huang, J. Krzywinski, T. Maxwell, M. Messerschmidt, and H.-D. Nuhn, Experimental Demonstration of Femtosecond Two-Color X-Ray Free-Electron Lasers, *Phys. Rev. Lett.* **110**, 134801 (2013).
- [65] R. Bonifacio, L. De Salvo, P. Pierini, N. Piovella, and C. Pellegrini, Spectrum, Temporal Structure, and Fluctuations in a High-Gain Free-Electron Laser Starting from Noise, *Phys. Rev. Lett.* **73**, 70 (1994).
- [66] T. Driver, S. Li, E. G. Champenois, J. Duris, D. Ratner, T. J. Lane, P. Rosenberger, A. Al-Haddad, V. Averbukh, T. Barnard *et al.*, Attosecond transient absorption spooktscopy: A ghost imaging approach to ultrafast absorption spectroscopy, *Phys. Chem. Chem. Phys.* **22**, 2704 (2020).
- [67] S. Li, T. Driver, A. Al Haddad, E. G. Champenois, M. Agåker, O. Alexander, T. Barillot, C. Bostedt, D. Garratt, L. Kjellsson *et al.*, Two-dimensional correlation analysis for x-ray photoelectron spectroscopy, *J. Phys. B: At. Mol. Opt. Phys.* **54**, 144005 (2021).
- [68] F. Calegari, D. Ayuso, A. Trabattoni, L. Belshaw, S. De Camillis, F. Frassetto, L. Poletto, A. Palacios, P. Decleva, J. B. Greenwood *et al.*, Ultrafast charge dynamics in an amino acid induced by attosecond pulses, *IEEE J. Sel. Top. Quantum Electron.* **21**, 1 (2015).
- [69] D. Ayuso, A. Palacios, P. Decleva, and F. Martín, Ultrafast charge dynamics in glycine induced by attosecond pulses, *Phys. Chem. Chem. Phys.* **19**, 19767 (2017).
- [70] M. Lara-Astiaso, A. Palacios, P. Decleva, I. Tavernelli, and F. Martín, Role of electron-nuclear coupled dynamics on charge migration induced by attosecond pulses in glycine, *Chem. Phys. Lett.* **683**, 357 (2017).
- [71] M. Lara-Astiaso, M. Galli, A. Trabattoni, A. Palacios, D. Ayuso, F. Frassetto, L. Poletto, S. De Camillis, J. Greenwood, P. Decleva *et al.*, Attosecond pump-probe spectroscopy of charge dynamics in tryptophan, *J. Phys. Chem. Lett.* **9**, 4570 (2018).
- [72] J. Delgado, M. Lara-Astiaso, J. González-Vázquez, P. Decleva, A. Palacios, and F. Martín, Molecular fragmentation as a way to reveal early electron dynamics induced by attosecond pulses, *Faraday Discuss.* **228**, 349 (2021).

- [73] J. Breidbach and L. S. Cederbaum, Universal Attosecond Response to the Removal of an Electron, *Phys. Rev. Lett.* **94**, 033901 (2005).
- [74] A. I. Kuleff, S. Lünemann, and L. S. Cederbaum, Ultrafast charge migration following valence ionization of 4-methylphenol: Jumping over the aromatic ring, *J. Phys. Chem. A* **114**, 8676 (2010).
- [75] A. I. Kuleff and L. S. Cederbaum, Ultrafast correlation-driven electron dynamics, *J. Phys. B: At. Mol. Opt. Phys.* **47**, 124002 (2014).
- [76] M. Vacher, L. Steinberg, A. J. Jenkins, M. J. Bearpark, and M. A. Robb, Electron dynamics following photoionization: Decoherence due to the nuclear-wave-packet width, *Phys. Rev. A* **92**, 040502(R) (2015).
- [77] M. Vacher, M. J. Bearpark, M. A. Robb, and J. P. Malhado, Electron Dynamics upon Ionization of Polyatomic Molecules: Coupling to Quantum Nuclear Motion and Decoherence, *Phys. Rev. Lett.* **118**, 083001 (2017).
- [78] C. Arnold, O. Vendrell, and R. Santra, Electronic decoherence following photoionization: Full quantum-dynamical treatment of the influence of nuclear motion, *Phys. Rev. A* **95**, 033425 (2017).
- [79] C. Arnold, O. Vendrell, R. Welsch, and R. Santra, Control of Nuclear Dynamics through Conical Intersections and Electronic Coherences, *Phys. Rev. Lett.* **120**, 123001 (2018).
- [80] M. Borland, *Elegant: A Flexible SDDS-Compliant Code for Accelerator Simulation*, Tech. Rep. LS-287, TRN: US0004540 (Argonne National Lab, Illinois, 2000).
- [81] Z. Zhang, J. Duris, J. P. MacArthur, A. Zholents, Z. Huang, and A. Marinelli, Experimental demonstration of enhanced self-amplified spontaneous emission by photocathode temporal shaping and self-compression in a magnetic wiggler, *New J. Phys.* **22**, 083030 (2020).
- [82] S. Reiche, GENESIS 1.3: A fully 3D time-dependent FEL simulation code, *Nucl. Instrum. Methods Phys. Res., Sect. A* **429**, 243 (1999).
- [83] E. Prat, R. Abela, M. Aiba, A. Alarcon, J. Alex, Y. Arbelo, C. Arrell, V. Arsov, C. Bacellar, C. Beard *et al.*, A compact and cost-effective hard x-ray free-electron laser driven by a high-brightness and low-energy electron beam, *Nat. Photonics* **14**, 748 (2020).
- [84] R. Schoenlein, P. Abbamonte, F. Abild-Pedersen, P. Adams, M. Ahmed, F. Albert, R. A. Mori, P. Anfinrud, A. Aquila, M. Armstrong *et al.*, *New Science Opportunities Enabled by LCLS-II X-Ray Lasers*, Tech. Rep. SLAC-R-1053 (SLAC National Accelerator Laboratory, Menlo Park, CA, US, 2015).
- [85] M. Barbatti and K. Sen, Effects of different initial condition samplings on photodynamics and spectrum of pyrrole, *Int. J. Quantum Chem.* **116**, 762 (2016).
- [86] J. P. Dahl and M. Springborg, The Morse oscillator in position space, momentum space, and phase space, *J. Chem. Phys.* **88**, 4535 (1988).
- [87] M. J. Frisch, G. W. Trucks, H. B. Schlegel, G. E. Scuseria, M. A. Robb, J. R. Cheeseman, G. Scalmani, V. Barone, G. A. Petersson, H. Nakatsuji *et al.*, *Gaussian 16 Revision B.01*, Gaussian Inc., Wallingford CT (2016).
- [88] V. Yatsyna, D. J. Bakker, R. Feifel, A. M. Rijs, and V. Zhaunerchyk, Aminophenol isomers unraveled by conformer-specific far-IR action spectroscopy, *Phys. Chem. Chem. Phys.* **18**, 6275 (2016).
- [89] NIST Mass Spectrometry Data Center, William E. Wallace director, in *NIST Chemistry WebBook, NIST Standard Reference Database Number 69*, edited by P. Linstrom and W. Mallard (National Institute of Standards and Technology, Gaithersburg MD, 20899, 2021).
- [90] H. Bachau, E. Cormier, P. Decleva, J. E. Hansen, and F. Martín, Applications of *B*-splines in atomic and molecular physics, *Rep. Prog. Phys.* **64**, 1815 (2001).
- [91] D. Toffoli, M. Stener, G. Fronzoni, and P. Decleva, Convergence of the multicenter B-spline DFT approach for the continuum, *Chem. Phys.* **276**, 25 (2002).
- [92] R. van Leeuwen and E. J. Baerends, Exchange-correlation potential with correct asymptotic behavior, *Phys. Rev. A* **49**, 2421 (1994).
- [93] M. Stener, D. Toffoli, G. Fronzoni, and P. Decleva, Recent advances in molecular photoionization by density functional theory based approaches, *Theor. Chem. Acc.* **117**, 943 (2007).
- [94] S. E. Canton, E. Plésiat, J. D. Bozek, B. S. Rude, P. Decleva, and F. Martín, Direct observation of Young's double-slit interferences in vibrationally resolved photoionization of diatomic molecules, *Proc. Natl. Acad. Sci. USA* **108**, 7302 (2011).
- [95] D. Catone, M. Stener, P. Decleva, G. Contini, N. Zema, T. Prosperi, V. Feyer, K. C. Prince, and S. Turchini, Resonant Circular Dichroism of Chiral Metal-Organic Complex, *Phys. Rev. Lett.* **108**, 083001 (2012).
- [96] R. K. Kushawaha, M. Patanen, R. Guillemin, L. Journel, C. Miron, M. Simon, M. N. Piancastelli, C. Skates, and P. Decleva, From double-slit interference to structural information in simple hydrocarbons, *Proc. Natl. Acad. Sci. USA* **110**, 15201 (2013).
- [97] A. Ponzi, M. Sapunar, C. Angeli, R. Cimiraglia, N. Došlić, and P. Decleva, Photoionization of furan from the ground and excited electronic states, *J. Chem. Phys.* **144**, 084307 (2016).
- [98] K. Ueda, C. Miron, E. Plésiat, L. Argenti, M. Patanen, K. Kooser, D. Ayuso, S. Mondal, M. Kimura, K. Sakai *et al.*, Intramolecular photoelectron diffraction in the gas phase, *J. Chem. Phys.* **139**, 124306 (2013).
- [99] T. Moitra, S. Coriani, and P. Decleva, Capturing correlation effects on photoionization dynamics, *J. Chem. Theory Comput.* **17**, 5064 (2021).
- [100] G. te Velde, F. M. Bickelhaupt, E. J. Baerends, C. Fonseca Guerra, S. J. A. van Gisbergen, J. G. Snijders, and T. Ziegler, Chemistry with ADF, *J. Comput. Chem.* **22**, 931 (2001).
- [101] D. P. Chong, O. V. Gritsenko, and E. J. Baerends, Interpretation of the Kohn–Sham orbital energies as approximate vertical ionization potentials, *J. Chem. Phys.* **116**, 1760 (2002).
- [102] M. Lara-Astiaso, D. Ayuso, I. Tavernelli, P. Decleva, A. Palacios, and F. Martín, Decoherence, control and attosecond probing of XUV-induced charge migration in biomolecules. A theoretical outlook, *Faraday Discuss.* **194**, 41 (2016).
- [103] L. Klasinc, I. Novak, A. Sabljic, and S. P. McGlynn, Photoelectron spectroscopy of biologically active molecules 12 benzene-containing amides, *Int. J. Quantum Chem.* **13**, 251 (1986).